

Symmetry Breaking in Chemical Systems: Engineering Complexity through Self-Organization and Marangoni Flows

Sangram Gore^{1†}, Binaya Paudyal^{1†}, Mohamed Ali¹, Nader Masmoudi^{1,2},
Albert Bae³, Oliver Steinbock⁴, Azam Gholami^{1*}

¹Science Division, New York University Abu Dhabi, Abu Dhabi, UAE

²Courant Institute of Mathematical Sciences, New York University, New York, USA

³Lewis & Clark College, Portland, Oregon, USA.

⁴Department of Chemistry and Biochemistry, Florida State University
Tallahassee, Florida, USA

[†]These authors contributed equally to this work.

*Corresponding author: azam.gholami@nyu.edu.

Far from equilibrium, chemical and biological systems can form complex patterns and waves through reaction-diffusion coupling. Fluid motion often tends to disrupt these self-organized concentration patterns. In this study, we investigate the influence of Marangoni-driven flows in a thin layer of fluid ascending the outer surfaces of hydrophilic obstacles on the spatio-temporal dynamics of chemical waves in the modified Belousov-Zhabotinsky reaction. Our observations reveal that circular waves originate nearly simultaneously at the obstacles and propagate outward. In a covered setup, where evaporation is minimal, the wavefronts maintain their circular shape. However, in an uncovered setup with significant evaporative cooling, the interplay between surface tension-driven Marangoni flows and gravity destabilizes the wavefronts, creating distinctive flower-like patterns around the obstacles. Our experiments

further show that the number of petals formed increases linearly with the obstacle's diameter, though a minimum diameter is required for these instabilities to appear. These findings demonstrate the potential to 'engineer' specific wave patterns, offering a method to control and direct reaction dynamics. This capability is especially important for developing microfluidic devices requiring precise control over chemical wave propagation.

Introduction

Symmetry breaking is a fundamental concept in physics, biology and chemistry where small perturbations can lead to the emergence of complex structures and patterns from initially uniform states [1, 2]. In fluid dynamics, this phenomenon is exemplified by the transition from simple, laminar flows to intricate turbulent structures, driven by instabilities that disrupt the symmetry of the system. In biology, Alan Turing's reaction-diffusion theory proposes that the initial symmetry in embryos can be broken by the interaction of two diffusible molecules, whose dynamic interplay leads to the formation of complex patterns [3]. Similarly, in chemical systems like the Belousov-Zhabotinsky (BZ) reaction, symmetry breaking can give rise to a rich spectrum of spatio-temporal structures, such as rotating spirals and target waves as well as Turing patterns [4–21]. These patterns, resulting from the interplay between nonlinear reaction kinetics and diffusion, offer profound insights into the mechanisms of self-organization in both natural and synthetic systems [1, 22].

The interaction between chemical reactions and convective fluid motion, particularly through mechanisms such as Marangoni-driven flows, profoundly influences the formation and breakdown of complex spatio-temporal patterns [23, 24]. In pioneering studies on the BZ reaction [25–29], it was observed that in confined environments, chemical instabilities manifest themselves as propagating waves. In contrast, in systems with a free surface, the presence of

Marangoni flows lead instead to the formation of cellular structures [12, 30–40]. These flows are initiated by gradients in surface tension [39, 41], which might arise from either temperature variations or differences in solute concentrations across the fluid’s surface, causing the fluid to flow from regions of lower to higher surface tension. For instance, in the ferroin-catalyzed BZ reaction, Fe^{2+} complex has a higher surface activity than Fe^{3+} complex [41]. In an uncovered setup, where evaporative cooling is significant, the interplay of chemical waves, buoyancy-driven flows due to density gradients, and Marangoni flows due to surface tension gradients collectively influences the resulting chemo-hydrodynamic patterns [26, 29, 35, 36, 42–45].

Evaporation induced Marangoni flows can be intensified by introducing hydrophilic vertical or inclined obstacles within the reactive medium. The thin film rising along the outer surfaces of these obstacles evaporates more quickly than the bulk fluid, creating thermal/solutal surface tension gradients. The delicate balance between upward-driving surface tension forces and gravity-induced downward motion leads to undulations at the fluid interface, potentially developing into finger-like patterns if the fluid becomes sufficiently unstable [46–52]. The obstacle’s geometry also affects the dynamics at the contact line region of thin films. A cylindrical obstacle introduces unique conditions, such as azimuthal curvature and periodic boundary conditions, absent in flat obstacles [52]. This periodicity ensures that an integer number of fingers can form along a cylinder, a condition that is not required for a flat obstacle, and the smallest number of fingers that can form along the contact line of a cylinder is one [52].

Building on these groundworks, our study presents a novel approach to explore the intricate interaction between evaporation driven Marangoni flows and chemical waves in the modified BZ reaction in the presence of hydrophilic obstacles. We observe that in a covered experimental setup with minimal evaporative cooling, the obstacles act as focal points that consistently emit synchronous circular waves and maintain their shape over multiple cycles. In contrast, thermal/solutal driven Marangoni flows in an uncovered setup, where evaporative cooling is more

pronounced, trigger a fingering instability that leads to the formation of distinct flower-like wave patterns. Significantly, the number of petals increases with the diameter of the obstacles, and a minimum threshold value for the diameter is required for this instability to occur. We performed numerical simulations of a reaction-diffusion model to explain the observed wave dynamics and gain deeper insights into the underlying mechanisms.

Results

Experimental Results

Our quasi 2D setup consists of a periodic array of millimeter-sized PDMS-based cylindrical obstacles (see Fig. 1A and Fig. S1) that influence the spatio-temporal dynamics of chemical waves in the modified BZ reaction. This version of the BZ reaction (CHD-BZ) uses 1,4-cyclohexanedione as a bubble-free organic substrate and Fe(II)-[batho(SO₃)₂]₃ as a high-absorbance redox catalyst/indicator [53–59]. The PDMS has undergone plasma treatment to make it hydrophilic, which allows the fluid to climb up around these obstacles, as illustrated in Fig.1B. We observe circular oxidation waves that initiate almost synchronously at the pillars, spreading outward at a speed of approximately 7 mm/min and recurring every 45 sec (see Fig. 1). When these waves meet, they mutually annihilate each other. The time evolution of these waves is significantly affected by whether the setup is covered or uncovered, which alters the evaporation rate of the liquid. We discuss the results for both the setups below.

Covered setup: Circular waves initiate synchronously at the pillars and maintain their circular shape

In a covered setup, chemical waves begin nearly simultaneously on the pillars, with a wave period of about 45 sec, and maintain their circular shape across multiple wave cycles (Fig. 1C-D and Video 1). A space-time plot along an arbitrary line crossing the obstacles illustrates

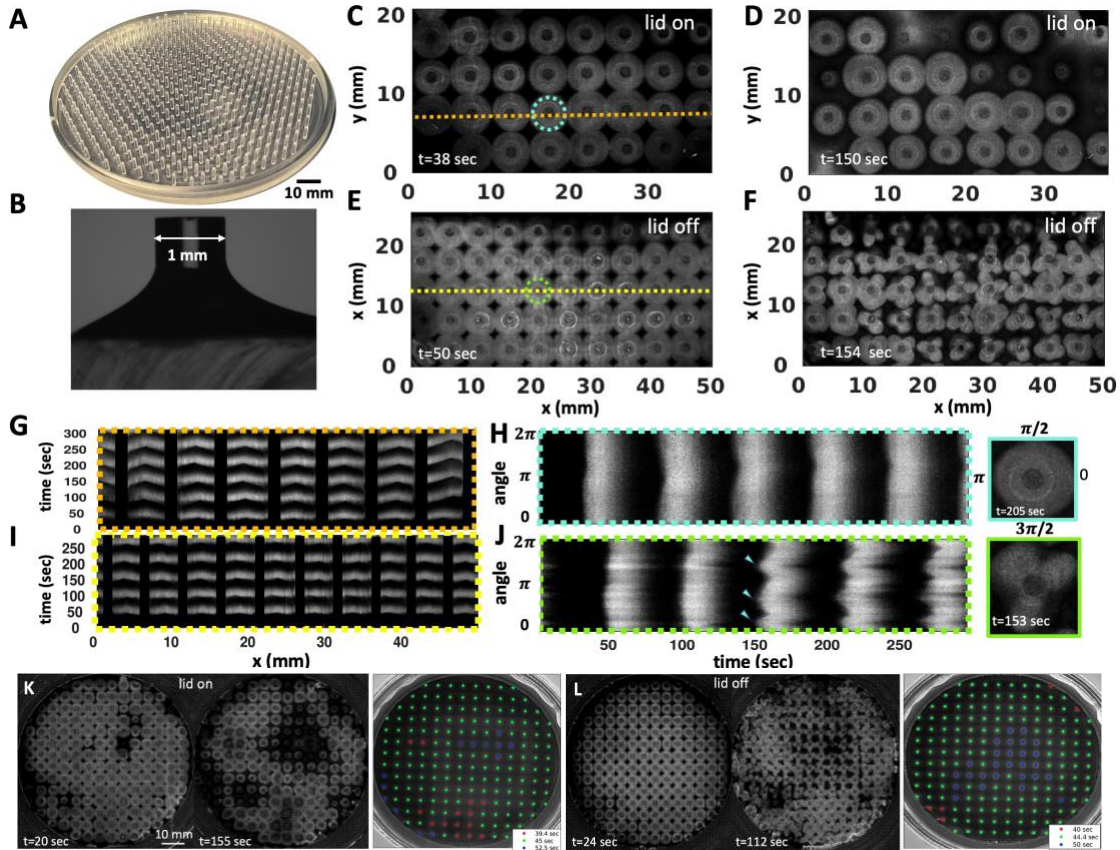


Figure 1: Wave dynamics in a covered versus an uncovered setup. (A) A standard experimental setup featuring a periodic arrangement of PDMS-based cylindrical obstacles designed to fit within a 10 mm Petri dish. (B) A side view depicting the fluid profile around an exemplary hydrophilic pillar. (C-D) Top views of concentric chemical waves in a covered setup, captured at two distinct times, show the waves initiating almost simultaneously at the pillars and spreading outward. The waves retain their circular shapes over time. (E-F) Top views of chemical waves captured at two distinct times in an uncovered setup: initially, concentric waves form around the obstacles (E), and later, the wavefronts fracture to create flower-like patterns (F). (G) A space-time plot along the orange line indicated in (C) demonstrates that the pillars serve as the wave centers. Black bars show the position of the obstacles. (H) A space-time plot traced along the cyan-colored circle shown in (C) illustrates that the circular waves retain their shape through multiple wave cycles. (I) The space-time plot along the yellow line shown in (E). (J) The space-time diagram along the green circle indicated in (E) illustrates that after two cycles of circular waves, the wavefronts break. In this experiment, where pillars are 1 mm in diameter, 3 mm tall, and spaced 5 mm apart, most pillars develop three petals. (K-L) Images displaying the entire Petri dish from two separate experiments: one covered and the other uncovered. The color-coded wave period around each pillar is also shown in seconds. The timestamps reflect the elapsed time since the start of recording, which began shortly after the chemical solution was introduced into the setup. These images are typical of at least 50 experiments.

that they serve as wave centers (Fig. 1G). Additionally, to visualize the wave dynamics over several cycles, we compiled the light intensity data along a circle surrounding an arbitrary pillar, confirming that the wavefronts consistently retain their circular form (Fig. 1H). Figure 1K and video 2 present a separate experiment where the entire Petri dish is imaged, demonstrating similar wave dynamics. Fourier analysis of the waves emanating from the obstacles indicates that the majority have a periodicity of 45 sec (Fig. S2A-D).

Uncovered setup: Circular waves begin synchronously at the pillars and eventually evolve into flower-like patterns

In an uncovered setup, where evaporation is more significant, the obstacles continue to act as centers that emit synchronous concentric waves (Fig. 1E, I and video 3). However, after approximately two cycles of these circular waves, an instability in the wavefront becomes apparent: the circular wavefronts fragment, leading to the formation of striking flower-like patterns (see Fig. 1F, J). Figure 1L and video 4 present a separate experiment where the entire Petri dish is imaged, demonstrating similar wavefront instability. Similar to a covered setup, Fourier analysis shows that the waves originating from the obstacles typically have a periodicity of about 45 seconds (see Fig. S2E-H).

Our experimental findings indicate that the number of petals is influenced by the diameter of the pillars. Typically, pillars with a diameter of 1 mm form three petals (Fig. 1F), while those with a diameter of 1.5 mm often produce four petals (Figs. 2-3), and pillars measuring 3.8 mm in diameter generate seven to eight petals (Fig. 4). Figure 2 presents an illustrative experiment where the pillar diameters alternate between 1 mm and 1.5 mm across neighboring rows, with the top row featuring pillars of 1.5 mm in diameter. In this setup, the 1 mm pillars typically form patterns with three petals, whereas the 1.5 mm pillars display flower patterns consisting of four petals (Fig. 2B-F and video 5). Interestingly, we noted that the number of petals can change over time, as illustrated in Fig. 2F. In a related observation, Fig. 3 depicts an experiment where, after

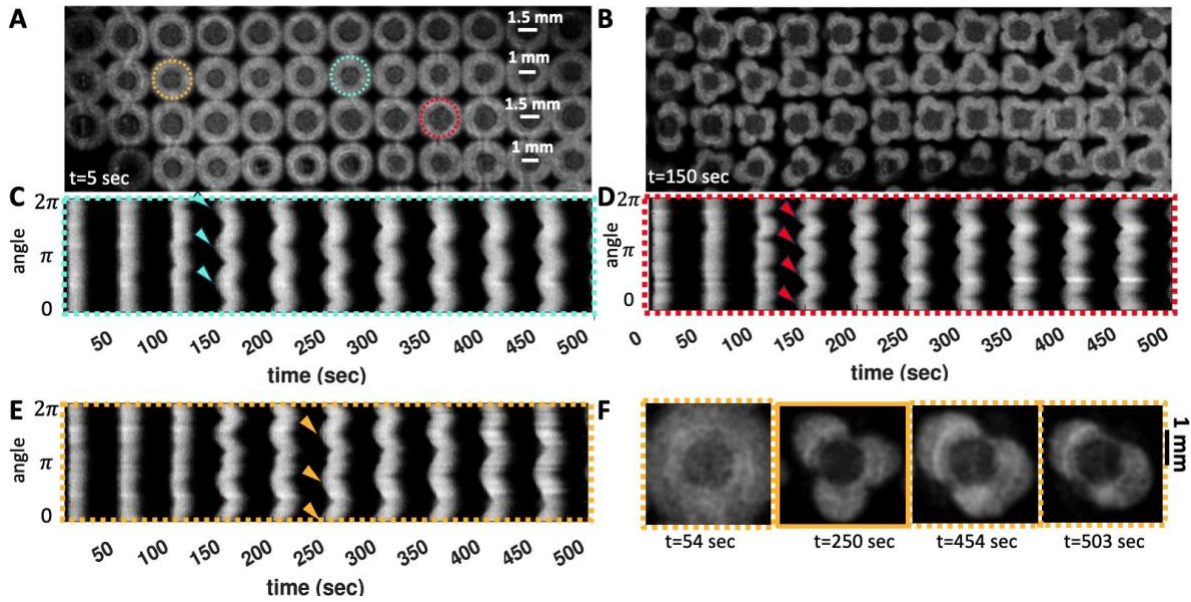


Figure 2: Number of petals depends on the pillar diameter and can vary over time. (A-B) Top views of chemical waves captured before and after the onset of instability in an experiment where pillar diameters alternate between rows, with 1.5 mm pillars in the top row and 1 mm pillars in the second row. Pillars with a diameter of 1.5 mm generally develop four petals, whereas those with a diameter of 1 mm typically produce three petals. **(C-E)** Space-time plots along the highlighted circles in panel (A) illustrate the progression of the instability. **(F)** An example of a pillar that initially developed three petals, but over time, two of the petals merged.

two cycles of circular wavefronts, the wavefronts around the pillars break. Initially, four petals form, but as time progresses, a fifth petal develops (Fig. 3C). The synchronization between the waves initiated at different pillars is demonstrated through a phase map calculated using the Hilbert transform (see Materials and Methods), as shown in Figs. 3A-B. In this experiment, where we have captured images of the entire small Petri dish, the waves initiated at the PDMS boundary also exhibit wavefront instability, similar to those observed at the pillars (see Fig. 3D and video 6).

To unravel the mechanisms (i) governing the formation of synchronous circular waves around the pillars and (ii) contributing to the instability of the wavefront in an uncovered setup,

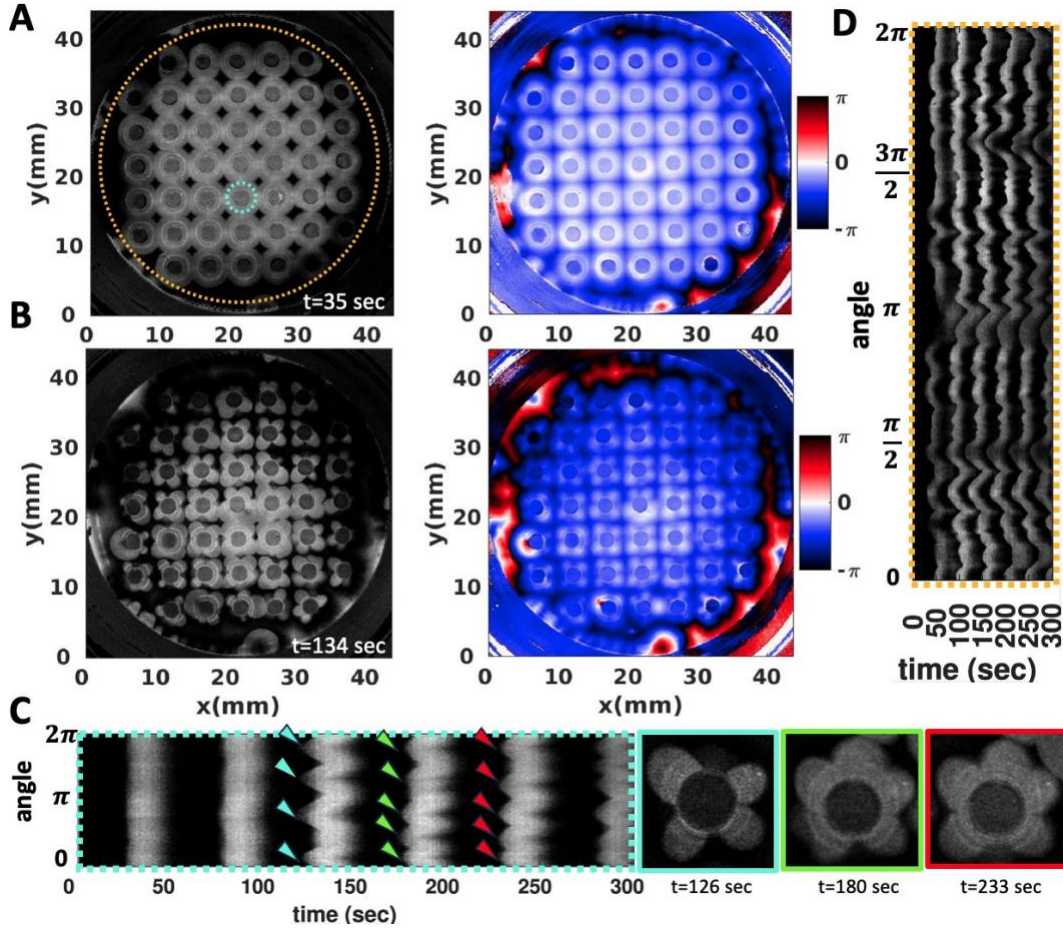


Figure 3: **Wavefront instability at the boundary in an uncovered setup.** (A-B) Pillars with a diameter of 1.85 mm typically form four petals. The color-coded phase map, generated using Hilbert transform, indicates that the pillars simultaneously act as wave centers. (C) A space-time plot along the cyan-highlighted circle in panel (A) shows the development of the instability, with a noticeable evolution in the number of petals over time. The wave period is 50 sec. (D) A space-time plot along the orange-highlighted circle demonstrates the wavefront instability that also manifests at the PDMS wall on the periphery. This experiment is conducted in a small Petri dish.

we began by examining the hypothesis that the permeability of PDMS to bromine gas (and potentially other chemicals) facilitates wave formation on the pillars, an idea supported by literature [60–62]. To test this possibility, we conducted experiments using PDMS pillars coated with a thin layer of gold (approximately 200 nm thick, see Fig. S1E). Contrary to expectations,

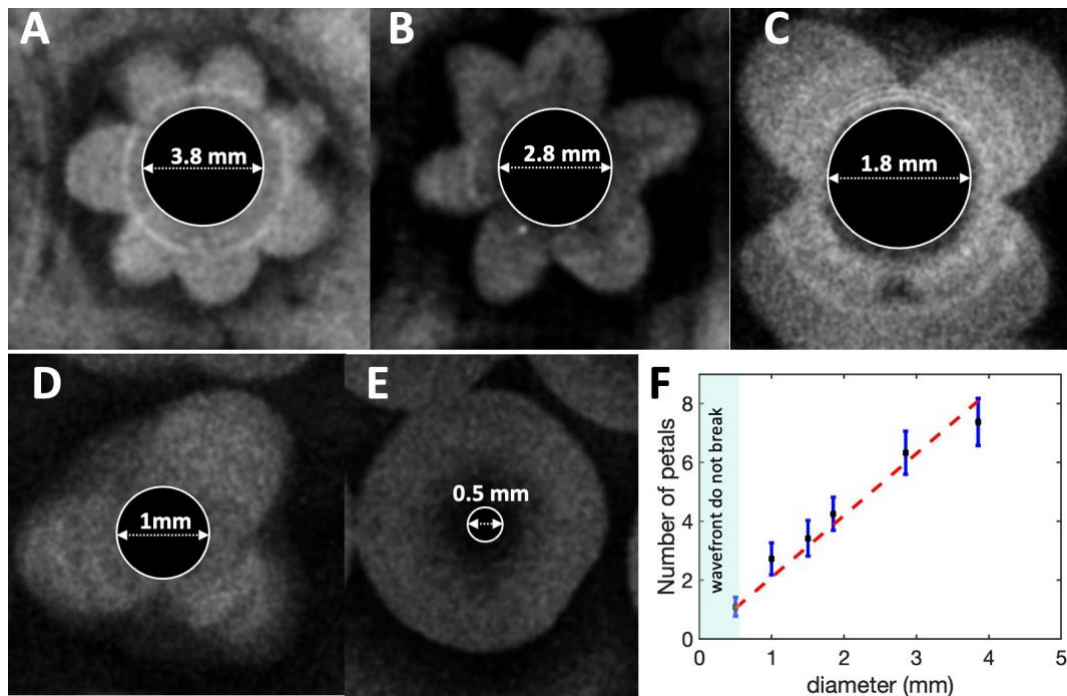


Figure 4: **Effect of the pillar diameter on the number of petals.** (A-D) As the pillar diameter decreases, so does the number of petals formed. For instance, pillars with a diameter of 3.8 mm typically develop around 7 petals, while those with a diameter of 2.8 mm produce about 6 petals. This number drops to 4 petals for pillars with a diameter of 1.8 mm, and further reduces to 3 petals for those with a diameter of 1 mm. (E) Pillars with a diameter of 0.5 mm exhibit no wavefront instability, which verifies that there is a minimum pillar perimeter required for such instability to develop. (F) The number of petals increases linearly with the diameter of the pillar. Below a critical diameter, wavefronts do not break and remain circular.

the pillars continued to function as centers for synchronous wave activity even with the gold coating, which blocks chemical absorption. Additionally, we conducted experiments using obstacles made of acrylic (PMMA) with plasma treatment and observed that these pillars also functioned as centers for wave activity (Fig. 5A-C and video 7). These results confirm that the absorption of chemicals into PDMS is not the primary mechanism driving the formation of concentric waves around the obstacles.

Next, we explored the impact of the thin liquid layer ascending the PDMS-made pillars,

which are hydrophilic due to plasma treatment. Our investigation involved several experimental approaches. Initially, we conducted experiments with pillars that had not undergone plasma treatment and observed that most of the pillars did not act as centers for wave generation (see Fig. S3 and video 8). Subsequently, we decreased the height of the pillars from 3 mm to 1 mm, ensuring that these shorter pillars were submerged to the same fluid level. We noted that the submerged pillars also did not act as wave centers (video 9). Lastly, to determine if the generation of circular waves around the pillars was influenced by the proximity of adjacent pillars, we conducted tests with a solitary pillar. As depicted in Fig. S4 and video 10, this isolated pillar also became a center for wave activity and further demonstrated wavefront instability in an uncovered setup. These experiments collectively affirm that the climbing liquid layer on the pillars is crucial in the generation of synchronous circular waves.

Experimental evidence of a fingering instability

As described earlier, our experiments reveal that the climbing film on the external surfaces of cylindrical pillars significantly influences the formation of synchronous circular waves and wavefront instability. We observe that wavefront instability occurs primarily in uncovered experimental setups where evaporation is more pronounced than in covered setups. It is reasonable to suggest that the thin, ascending liquid layer evaporates quicker than the thicker parts, creating a minor temperature/concentration gradient. This gradient induces a surface tension gradient, which in turn generates Marangoni flows. Our hypothesis that waves originate from the thin ascending fluid layer is supported by our observations in Fig. 5, using a PMMA mold with square wall boundaries. The side view of the waves confirms that they initiate at the thin film in the contact region, which wets the wall boundary, and then travel downward (video 11). Importantly, in an uncovered setup, the downward-traveling wave along the wall boundary initially maintains a planar form but eventually breaks into fingers at later times (Fig. 5B-C).

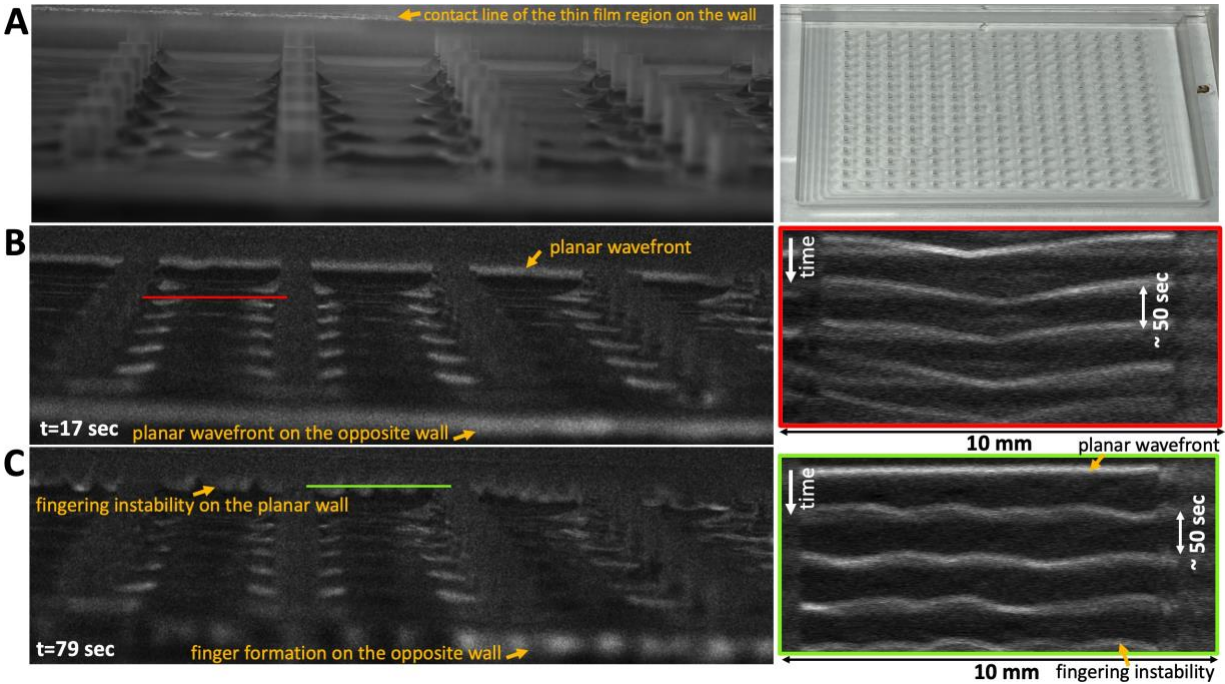


Figure 5: **Experiments with PMMA-made obstacles.** (A) Side view of the cylindrical obstacle array made from PMMA, with walls forming a square boundary. The fluid climbs up the plasma-treated hydrophilic obstacles as well as the wall boundary. (B) Images are subtracted every 3 seconds to better visualize the wavefronts initiating in the thin film region, wetting the pillars and the walls, and traveling downward. The obstacles act as wave centers, as shown in the space-time plot in the red box, which stacks up light intensity along the red line. (C) Initially, the wavefronts are planar along the wall and circular around the pillars, but they rapidly deform, developing into finger-like patterns. This wavefront instability on the wall is clearly visible in the space-time plot in the green box, created by stacking up the light intensity along the green line on the wall boundary. These images are representative of at least 10 experiments.

This fingering instability is similarly visible in Fig. 6E with PMMA-based triangular obstacles within square wall boundaries. Lastly, we note that the initiation of waves at the ascending thin film is consistent with a separate experiment in which the Petri dish was slightly tilted [32]. In this setup, we observed that synchronization waves initially appeared in regions with lower fluid thickness and subsequently propagated toward areas with higher fluid thickness (see Fig. S5A-B and video 12).

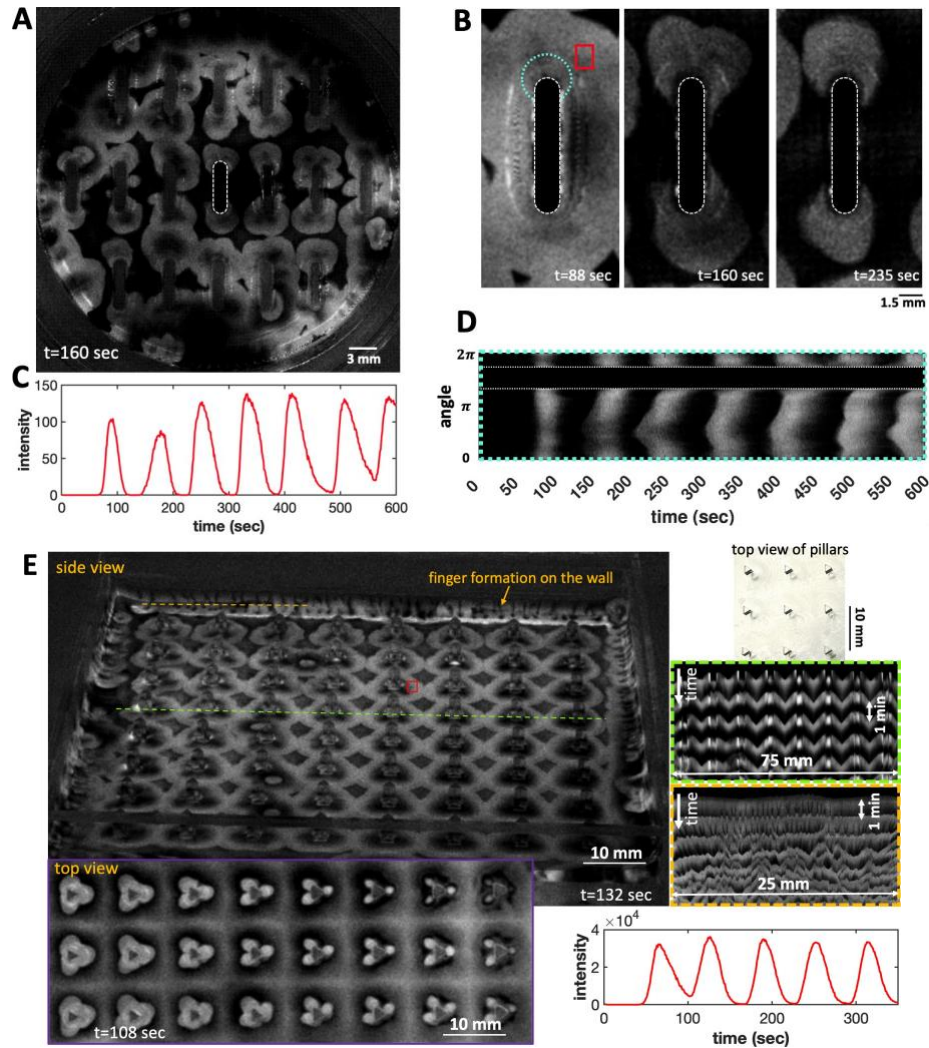


Figure 6: **Experiments with rounded rectangular obstacles and triangular obstacles.** (A) In an experiment examining the impact of evaporation, PDMS-made obstacles with a rectangular body and rounded ends were used. (B) The sequence of wave pattern of the highlighted pillar in panel (A) indicates that instability mainly arises at the curved ends. (C) Oscillations of light intensity averaged over the red box shown in panel (B). (D) A space-time plot along the circular path marked in cyan in panel (B) illustrates the progression of wavefront instability. (E) A side view of an experiment featuring triangular PMMA obstacles within a square boundary, where waves predominantly initiate at the sharp edges. Space-time plots along the green and orange lines are also shown. The intensity averaged over the red box shows oscillations of 60 seconds. Notably, the chemical fingers are clearly visible along the wall.

Literature reveals that Marangoni-driven thin films on planar or curved substrates exhibit a complex array of dynamics [49, 52, 63], dependent on the flat upstream film thickness trailing the advancing front. The thickness of this film is influenced by the meniscus curvature at the fluid source and the interplay of the thermal/solutal induced surface tension gradient with gravity. It is also important to note that surface tension gradients, which lead to Marangoni flows, may also arise from chemical concentration gradients. These gradients often develop due to the evaporation of more volatile chemical components within the ascending thin film, similar to what occurs in the tear of wine phenomenon [64]. The interplay between Marangoni flows and gravity can disrupt the contact lines, evolving into a finger pattern. Specifically, the linear stability analysis in Ref. [52] correlates linearly the number of fingers with the cylindrical pillar's perimeter, aligning with our findings (see Fig. 4). This analysis also suggests a minimum pillar diameter threshold below which fingering instability does not occur. To validate this, we reduced the pillar diameter to 0.5 mm in our uncovered setup experiments, observing that the wavefronts remained nearly circular (see Fig. S6).

Furthermore, we tested the impact of evaporation on fingering instability using obstacles with a rectangular geometry and circular ends (see Fig. 6A-D). Given the increased surface area at the curved boundaries, we anticipated a higher evaporation rate here, which likely triggers the fingering instability predominantly at these locations, a hypothesis supported by our observations. A similar pattern was noted in our experiments with obstacles of triangular cross-section, where waves primarily started at the sharp boundaries (Fig. 6E). Remarkably, we observed that during our experiments involving multiple cycles of covering and uncovering the setup, the wavefronts, which exhibit flower-like patterns when the setup is uncovered, revert to their circular form once the setup is covered again, and vice versa (video 13). Also, we conducted a control experiment using an uncovered, plasma-treated glass Petri dish without any obstacles (refer to Fig. S7). Interestingly, we observed wavefront instability at the glass boundary, which

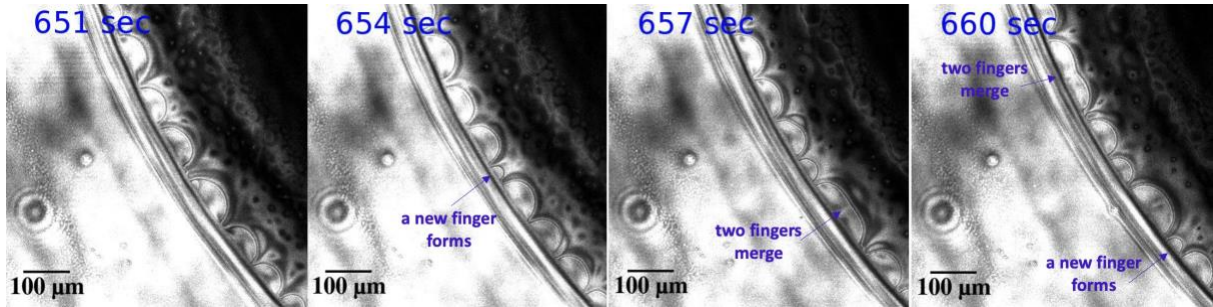


Figure 7: **Symmetry breaking in an evaporating CHD-BZ droplet.** A droplet of volume $2.5 \mu\text{l}$ is deposited on a hydrophobic glass substrate. After about 500 sec, the azimuthal symmetry breaks and spots form at the rim evolving over time ($T = 22^\circ\text{C}$, $\text{RH} = 40\%$, $\theta_0 = 12^\circ$). The images are captured in the reflection mode of a confocal microscope; see also video 14.

closely resembled the phenomena observed at the PDMS wall in Fig. 3 and PMMA wall in Fig. 5. Overall, these experiments confirm that the thin layer of climbing fluid at the boundary is critical for initiating waves, and that evaporation significantly contributes to the wavefront instability.

Our last experiment that clearly proves the important role of evaporation in spontaneous breaking of azimuthal-symmetry is an evaporating CHD-BZ droplet. The preferential evaporation of more volatile chemical components at the rim can contribute to the segregation of other chemicals near the rim and eventually break the azimuthal symmetry. Figure 7 shows spot formation near the boundary of a droplet. A similar effect has been reported in water/1,2-hexanediol binary drops in Refs. [65–68], where 1,2-hexanediol micro-droplets nucleate at the rim of the droplet.

Numerical Simulations

We conducted numerical simulations using the Tyson-Fife model [69] in two dimensions to understand wave dynamics observed in the experiments (refer to Materials and Methods for details). In our simulations, we applied a boundary condition based on the hypothesis that the

inhibitor w is depleted at the outer surface of the obstacles due to evaporation. This assumption is supported by experimental observations where the fluid ascends the hydrophilic pillars, forming a thin film subject to more rapid evaporation compared to the bulk solution. Simulation results, as displayed in Fig. 8, set the inhibitor w to zero at the locations of the pillars. The depletion of inhibitor near the obstacles results in an increased concentration of activator (bromate) available to oxidize the metal catalyst, thus initiating oxidation waves at the obstacles. This is in agreement with our experimental observations.

Next, we investigated how fingering patterns affect wave dynamics by analyzing the impact of an uneven angular distribution of w around the obstacles (refer to Materials and Methods for more information). The results of this analysis are presented in Fig. 8C and Fig. S9. Depending on the asymmetry introduced, a varying number of petals emerge following at least one initial cycle of circular waves. Remarkably, even with a set asymmetry of w near the obstacles, the orientation and size of the petals can vary as the simulation progresses. To emulate the experimental setup of a tilted Petri dish (Fig. S5A-B), we adapted the Tyson-Fife model to include a term that reflects a linear increase in fluid thickness (refer to Materials and Methods). In line with our experimental findings, the waves initially emerge in areas with thinner fluid and then move toward regions with thicker fluid (Fig. S5C).

Discussion

In this study, we introduce a periodic array of hydrophilic cylindrical obstacles into the CHD-BZ reaction which quickly turn them into synchronous centers of wave activity. The thin layer of chemical solution that ascends the outer surface of the obstacles plays a crucial role in enabling them to function as wave centers, effectively determining the spatial positioning of these centers (Fig. 1). While a single isolated obstacle can also serve as a wave center (Fig. S4), the presence of an obstacle array helps to prevent the formation of other random wave centers. In a covered

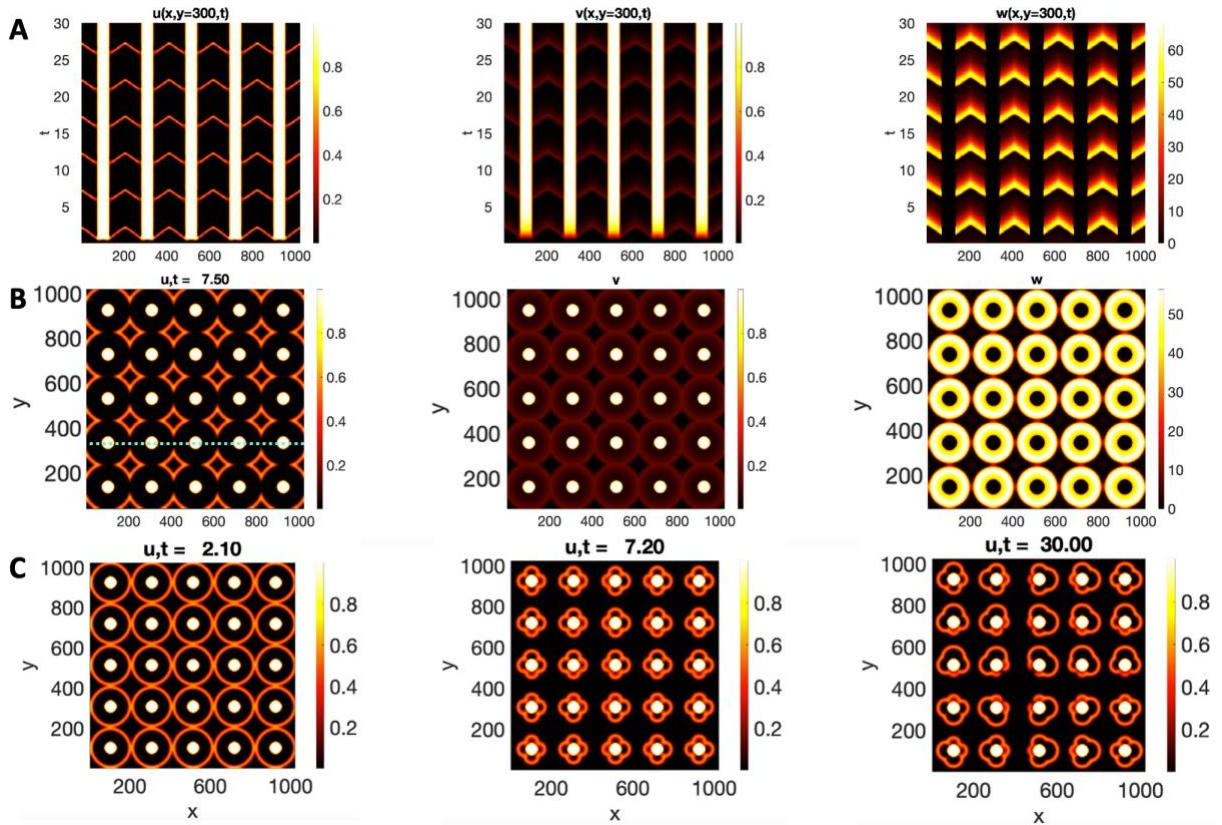


Figure 8: **Numerical simulations of the Tyson-Fife model** (A) The space-time plot along the line marked in panel (B) illustrates that the obstacles become wave centers. (B) shows an image of the circular waves emanating from the obstacles at dimensionless time $t = 7.5$. Time and space are in arbitrary units. (C) Simulations incorporating an asymmetric distribution of the inhibitor w around the obstacles demonstrate wavefront instability at different time points. Only concentration of activator u is shown (see also Fig. S9).

setup where evaporation is minimal, wavefronts maintain their circular shapes through multiple wave cycles. Conversely, in an uncovered setup where evaporation plays a substantial role, Marangoni-driven fingering instability occurs and wavefronts break, leading to the formation of striking flower-like wave patterns (Fig. 1). The number of petals formed is linearly proportional to the diameter of the obstacles (Fig. 4), and a minimum diameter is necessary for this instability to occur (Fig. S6).

The behavior of a film climbing the exterior of a vertical or an inclined wall, influenced by the opposing forces of a thermally/chemically driven surface tension gradient and gravity, is extensively explored in the literature through numerical analysis using a thin-film model (see review articles [46–48] and references therein). In the case of a cylindrical obstacle, these models depend on three parameters: the cylinder radius, the upstream film height, and the downstream precursor film thickness. As the cylinder radius approaches infinity, the model converges to the scenario of a Marangoni-driven film ascending a vertical plate [49–51,70]. Ref. [52] investigates the stability of the contact line by introducing an infinitesimal two-dimensional perturbation to the traveling wave solution, characterized by sinusoidal variations in the azimuthal direction. Through linear stability analysis, the study determines that the traveling wave (the so called Lax shock) is unstable to long-wave perturbations at the contact line. Given the periodic nature of the contact line in the azimuthal direction, only an integer number of fingers can form along it. The analysis identifies the most unstable mode and a neutrally stable cutoff mode, beyond which all modes are stable. These modes increase linearly with the cylinder radius, indicating that the number of fingers formed along the contact line correlates with the cylinder’s circumference. There exists a critical cylinder radius below which the contact line remains stable, with no fingers forming. Our experimental results align with these theoretical findings. In future, we aim to expand the numerical analysis from Ref. [52] to include the rounded rectangular obstacle geometry (Fig. 6), incorporating an asymmetric evaporation rate that results in an asymmetric surface tension gradient. Additionally, we will integrate the thin film equations from Ref. [52] with the reaction-diffusion equations to fully capture the dynamics of both the fluid flow and chemical components in the thin film surrounding the obstacles.

In our experiments, by tilting the Petri dish, it is possible to selectively control which array of obstacles initially becomes the focal point for wave generation (Fig. S5A-B). As reported in Ref. [26] and consistent with our experiments, in a tilted Petri dish, waves originate in the thin-

ner areas of the fluid, where convective flows are negligible, and progress toward the thicker regions, where convective flows can develop due to evaporative cooling. They assumed that these convective flows generate a heterogeneous medium where the refractory tail of a preceding wave annihilates part of the following wavefront, resulting in segmented waves that curl inward to form spirals. Over time, a chaotic wave pattern develops. In another study to understand the role of the fluid thickness in an uncovered Petri dish, Rossi et al. [35] have demonstrated that for fluid layers thinner than 1.0 mm, the BZ system behaves predominantly as a pure reaction-diffusion system, and convective effects are negligible. In layers with an intermediate thickness of 1.0–3.0 mm (the fluid thickness in our experiments was about 1.5 mm), Marangoni instabilities dominate, allowing rippled waves to propagate without breaking, and segmented patterns are not observed. However, for layers thicker than 3.0 mm, buoyancy-driven flows become significant, and wave segmentation processes occur. Our experiment using an uncovered, plasma-treated glass Petri dish with a fluid thickness of 2 mm also revealed rippled wavefronts and Marangoni-driven mosaic patterns (Fig. S7A) [37–40]. We notice that at the boundary of the Petri dish, we observed a Marangoni-driven fingering instability, similar to the phenomena we see near the hydrophilic obstacles. Finally, in our experiments with an evaporating CHD-BZ droplet, we observed the formation of spots at the rim. To elucidate the underlying mechanism, identify the more volatile components, and determine which chemical elements are segregated at the boundary, additional comprehensive experiments are necessary. These studies are currently underway in our laboratory.

In summary, the insights gained from our study on the spatio-temporal dynamics of chemical waves influenced by a periodic array of cylindrical obstacles have several promising applications. By demonstrating that these obstacles can synchronize and direct wave propagation, we offer a method for engineering specific wave patterns, which is invaluable for the development of advanced microfluidic devices. Additionally, the ability to control wavefront shapes and in-

duce specific patterns such as flower-like structures through thermal Marangoni flows could be leveraged in materials science for creating structured surfaces with tailored properties. This approach could also optimize industrial processes involving thin films and coatings, enhancing efficiency in sectors ranging from electronics to biotechnology. Overall, our findings provide a strategic framework for manipulating chemical wave behaviors, paving the way for innovative applications in technology and manufacturing.

References

- [1] R. B. Hoyle, *Pattern formation: an introduction to methods* (Cambridge University Press, 2006).
- [2] H. Meinhardt, *Reports on Progress in Physics* **55**, 797 (1992).
- [3] A. M. Turing, *Bulletin of mathematical biology* **52**, 153 (1990).
- [4] A. Zaikin, A. Zhabotinsky, *Nature* **225**, 535 (1970).
- [5] I. R. Epstein, J. A. Pojman, *An introduction to nonlinear chemical dynamics: oscillations, waves, patterns, and chaos* (Oxford university press, 1998).
- [6] R. J. Field, R. M. Noyes, *The Journal of Chemical Physics* **60**, 1877 (1974).
- [7] J. J. Tyson, *The belousov-zhabotinskii reaction*, vol. 10 (Springer Science & Business Media, 2013).
- [8] O. Steinbock, V. Zykov, S. C. Müller, *Nature* **366**, 322 (1993).
- [9] A. T. Winfree, *Scientific American* **230**, 82 (1974).
- [10] O. Steinbock, Á. Tóth, K. Showalter, *Science* **267**, 868 (1995).

- [11] B. T. Ginn, O. Steinbock, *Physical review letters* **93**, 158301 (2004).
- [12] B. T. Ginn, B. Steinbock, M. Kahveci, O. Steinbock, *The Journal of Physical Chemistry A* **108**, 1325 (2004).
- [13] O. Steinbock, H. Engel, *Engineering Of Chemical Complexity* (World Scientific, 2013), pp. 147–167.
- [14] K. Suzuki, T. Yoshinobu, H. Iwasaki, *The Journal of Physical Chemistry A* **104**, 5154 (2000).
- [15] A. S. Mikhailov, K. Showalter, *Physics Reports* **425**, 79 (2006).
- [16] K. Agladze, J. P. Keener, S. C. Müller, A. Panfilov, *Science* **264**, 1746 (1994).
- [17] W. Guo, C. Qiao, Z. Zhang, Q. Ouyang, H. Wang, *Physical Review E—Statistical, Non-linear, and Soft Matter Physics* **81**, 056214 (2010).
- [18] V. S. Zykov, *Philosophical Transactions of the Royal Society A: Mathematical, Physical and Engineering Sciences* **376**, 20170379 (2018).
- [19] V. S. Zykov, *Simulation of wave processes in excitable media* (Manchester University Press, 1987).
- [20] B. Dúzs, P. De Kepper, I. Szalai, *ACS omega* **4**, 3213 (2019).
- [21] V. V. Yashin, A. C. Balazs, *Science* **314**, 798 (2006).
- [22] J. Halatek, E. Frey, *Nature Physics* **14**, 507 (2018).
- [23] A. De Wit, *Annual Review of Fluid Mechanics* **52**, 531 (2020).

- [24] M. Budroni, A. De Wit, *Chaos: An Interdisciplinary Journal of Nonlinear Science* **27** (2017).
- [25] K. Showalter, *The Journal of Chemical Physics* **73**, 3735 (1980).
- [26] K. Agladze, V. Krinsky, A. Pertsov, *Nature* **308**, 834 (1984).
- [27] S. C. Müller, T. Plesser, B. Hess, *Physicochemical Hydrodynamics: Interfacial Phenomena* pp. 423–433 (1988).
- [28] H. Miike, S. C. Müller, B. Hess, *Physical review letters* **61**, 2109 (1988).
- [29] H. Miike, S. C. Müller, B. Hess, *Chemical physics letters* **144**, 515 (1988).
- [30] S. Kai, H. Miike, *Physica A: Statistical Mechanics and its Applications* **204**, 346 (1994).
- [31] S. Kai, T. Ariyoshi, S. Inenaga, H. Miike, *Physica D: Nonlinear Phenomena* **84**, 269 (1995).
- [32] O. Inomoto, T. Ariyoshi, S. Inanaga, S. Kai, *Journal of the Physical Society of Japan* **64**, 3602 (1995).
- [33] I. R. Epstein, *et al.*, *Accounts of chemical research* **45**, 2160 (2012).
- [34] V. K. Vanag, I. R. Epstein, *Physical Chemistry Chemical Physics* **11**, 897 (2009).
- [35] F. Rossi, M. A. Budroni, N. Marchettini, J. Carballido-Landeira, *Chaos: An Interdisciplinary Journal of Nonlinear Science* **22** (2012).
- [36] F. Rossi, M. L. T. Liveri, *Ecological Modelling* **220**, 1857 (2009).
- [37] H. Miike, K. Miura, A. Nomura, T. Sakurai, *Physica D: Nonlinear Phenomena* **239**, 808 (2010).

- [38] K. Matthiessen, S. C. Müller, *Physical Review E* **52**, 492 (1995).
- [39] K. Matthiessen, H. Wilke, S. C. Müller, *Physical Review E* **53**, 6056 (1996).
- [40] M. A. Budroni, M. Masia, M. Rustici, N. Marchettini, V. Volpert, *The Journal of chemical physics* **130** (2009).
- [41] K. Yoshikawa, T. Kusumi, M. Ukitsu, S. Nakata, *Chemical physics letters* **211**, 211 (1993).
- [42] T. Plessner, H. Wilke, K. H. Winters, *Chemical physics letters* **200**, 158 (1992).
- [43] H. Wilke, *Physica D: Nonlinear Phenomena* **86**, 508 (1995).
- [44] L. Rongy, A. De Wit, *The Journal of chemical physics* **124** (2006).
- [45] D. Lohse, *Annual review of fluid mechanics* **54**, 349 (2022).
- [46] A. Oron, S. H. Davis, S. G. Bankoff, *Reviews of modern physics* **69**, 931 (1997).
- [47] D. Bonn, J. Eggers, J. Indekeu, J. Meunier, E. Rolley, *Reviews of modern physics* **81**, 739 (2009).
- [48] R. V. Craster, O. K. Matar, *Reviews of modern physics* **81**, 1131 (2009).
- [49] A. L. Bertozzi, A. Münch, X. Fanton, A. M. Cazabat, *Physical review letters* **81**, 5169 (1998).
- [50] A. L. Bertozzi, A. Münch, M. Shearer, *Physica D: Nonlinear Phenomena* **134**, 431 (1999).
- [51] A. Münch, A. Bertozzi, *Physics of Fluids* **11**, 2812 (1999).
- [52] L. B. Smolka, *Physical Review E* **96**, 043107 (2017).

- [53] I. Szalai, K. Kurin-Csörgei, M. Orbán, *Physical Chemistry Chemical Physics* **4**, 1271 (2002).
- [54] T. Bánsági Jr, O. Steinbock, *Physical review letters* **97**, 198301 (2006).
- [55] C. T. Hamik, N. Manz, O. Steinbock, *The Journal of Physical Chemistry A* **105**, 6144 (2001).
- [56] N. Manz, B. T. Ginn, O. Steinbock, *The Journal of Physical Chemistry A* **107**, 11008 (2003).
- [57] C. T. Hamik, O. Steinbock, *New Journal of Physics* **5**, 58 (2003).
- [58] T. Bánsági, O. Steinbock, *Chaos: An Interdisciplinary Journal of Nonlinear Science* **18** (2008).
- [59] T. Bánsági Jr, O. Steinbock, *Physical Review E* **76**, 045202 (2007).
- [60] M. E. Moustaka, *et al.*, *The Journal of Physical Chemistry B* **125**, 5937 (2021).
- [61] J. Sheehy, *et al.*, *The Journal of Physical Chemistry B* **124**, 11690 (2020).
- [62] P. R. Buskohl, R. A. Vaia, *Science advances* **2**, e1600813 (2016).
- [63] X. Fanton, A. Cazabat, D. Quéré, *Langmuir* **12**, 5875 (1996).
- [64] J. Fournier, A. Cazabat, *Europhysics Letters* **20**, 517 (1992).
- [65] C. Diddens, P. J. Dekker, D. Lohse, *arXiv preprint arXiv:2402.17452* (2024).
- [66] Y. Li, *et al.*, *Physical review letters* **120**, 224501 (2018).
- [67] Y. Li, *et al.*, *Journal of fluid mechanics* **899**, A22 (2020).

[68] Y. Li, P. Lv, C. Diddens, D. Lohse, *Journal of Fluid Mechanics* **946**, A37 (2022).

[69] J. J. Tyson, P. C. Fife, *The Journal of Chemical Physics* **73**, 2224 (1980).

[70] A. Hosoi, J. W. Bush, *Journal of fluid Mechanics* **442**, 217 (2001).

Acknowledgments

We gratefully acknowledge fruitful discussions with professors G. Shubeita, A. Narayanan, A. Rebane, O. Omelchenko, A. Pumir, D. Lohse and E. Frey. We also thank Dr. Rezgui for his crucial assistance with confocal microscopy, and V. Dhanvi and J. Govindan for their outstanding work in manufacturing the acrylic molds.

Author contributions:

S.G. and B.P. conducted the experiments, O.S. and A.G. designed and carried out the numerical simulations. A.G. conceived the idea, designed the experiments, analyzed the data, and wrote the first draft of the manuscript. All authors discussed the results and revised the manuscript.

Data and materials availability

All data needed to evaluate the conclusions in the paper are present in the paper and/or the Supplementary Materials. Additional data related to this paper may be requested from the authors.

Supplementary materials

Experimental methods

Chemical preparation

The following chemicals and materials were used in this study. Sodium Bromate (NaBrO_3), Sodium Bromide (NaBr), Conc. Sulfuric acid (Conc. H_2SO_4), Malonic acid [$\text{CH}_2(\text{COOH})_2$], 1,4-Cyclohexanedione, Ferrous sulfate, 1,10-phenanthroline was provided by sigma and used without any further purification. Ferroin was synthesized by mixing Ferrous sulfate hexahydrate and 1,10-phenanthroline in 1:3 molar ratio. For CHD-BZ experiments different concentration of the stock solutions were prepared in dH_2O . Solution A: (494.58 mM solution of sodium bromate) Solution B: (891.9 mM solution of 1,4-Cyclohexanedione) Solution C: (971.9 mM solution of NaBr). A mixture was prepared in a beaker by combining 9 mL of solution A with 1.5 mL of solution B, which was then homogenized using a magnetic stirrer. Following this, 1.5 mL of the Ferroin indicator was added to the mix. Under a chemical fume hood, 0.8 mL of solution C was cautiously introduced to the reaction. The stirring continued for an estimated 1 hour and 45 minutes. Subsequent to this phase, an additional 1.5 mL of Ferroin was incorporated into the mixture. The stirring persisted at a controlled temperature of 23°C for a further 30 minutes, after which it was halted. Attention was then given to the mixture for any signs of color transformation, signaling the start of wave propagation, typically observed 3.5 to 4 hours post the initial mixing process. Following the onset of color change, the CHD-BZ reaction mixture was transferred to a plasma-treated PDMS mold featuring an array of macro-pillars, as specified in Fig. S1A. These pillars, typically 1 mm in diameter and 3 mm high, are arrayed in a square grid with 5 mm spacing. In experiments with variable pillar dimensions and spacings, the volume of the CHD-BZ solution was adjusted to ensure a liquid height of about 1.5 mm, thus avoiding submergence of the pillars. Upon pouring, the solution was swirled

gently until the mixture achieved a brown color. The Petri dish was then positioned undisturbed beneath a camera to record the wave propagation, under the illumination of white LED light. In some experiments, a smaller, modified 50 mm Petri dish was used, and the volume of the CHD-BZ solution was correspondingly reduced to 1.5 mL to maintain the same liquid height. It's important to note that in our standard setups, unless specified otherwise, the pillars do not submerge in the chemical solution. The hydrophilic nature of plasma-treated PDMS causes a thin layer of liquid to ascend the pillars (Fig. 1B), altering the liquid surface near the obstacles as depicted in Fig. S1B.

For some experiments, the surface of the PDMS was coated with a 20 nm titanium layer and then with a pure gold layer. This was done using a Physical Vapor Deposition (PVD) technique with the Lesker Proline PVD 75 apparatus, rotating the substrate four times to achieve uniform coverage on the PDMS pillars' surfaces.

Image Processing

The wave period is roughly 45 sec, and we capture images of the chemical waves at a rate of 1 frame per second across multiple wave cycles. To minimize spatial noise, we average the captured images over several wave cycles, typically 6-8, and then subtract each individual image from the time-averaged image. After this, we apply a Gaussian blur filter and use a customized MATLAB code to perform the Hilbert transform, which helps us calculate the phase map. This code is provided in the Supplementary Information.

Numerical methods

We used the three-component Tyson-Fife model [69] to simulate our experimental system. The model focuses on the essential dynamics of the reaction by reducing the full chemical mechanism to a manageable number of reactions and variables. It typically includes the inhibitor w

which changes on the fastest time scale, activator u which is the second fastest variable, and the slow varying inhibitor v . The variables u , v and w represent the concentrations of bromous acid (HBrO_2), an oxidized form of the catalyst (such as ferroin Fe^{3+}), and bromide ions (Br^-), respectively. The set of equations for activator u and two inhibitors v and w are:

$$\frac{du}{dt} = D\nabla^2 u + \frac{1}{\epsilon}(aw - uw + u - u^2), \quad (1)$$

$$\frac{dv}{dt} = u - v, \quad (2)$$

$$\frac{dw}{dt} = \frac{1}{\epsilon'}(-aw - uw + bv), \quad (3)$$

where $\epsilon' \ll \epsilon \ll 1$, $a \ll 1$ and $b \simeq 1$. The parameters used are as follows: $D = 1$, $\epsilon = 0.05$, $\epsilon' = 0.001$, $b = 2.5$, $a = 0.002$. We note that at $b = 2.5$, the system is in the excitable state. The dimensions of the simulation box are chosen to be $N_x = N_y = 1023$. The positions of the pillars on a square lattice are determined by x and y coordinates that meet the condition: $0.5[1 + \cos(k(x - y) \cos(\pi/4)) * \cos(k(x + y) \cos(\pi/4))] \leq 0.1$, where k^{-1} representing the spacing between the pillars, is chosen to be $N_x/(6\pi)$. The concentration of inhibitor w is set to zero inside the pillars.

In the simulations featuring an asymmetric distribution of w around the pillars, we model the concentration of w in a narrow ring around the pillars as: $w(x, y) = \alpha[1 + \cos(k'(x - y) \cos(\pi/4)) * \cos(k'(x + y) \cos(\pi/4))]$, where k' is arbitrarily set to $\pi/10$ and $\alpha = 0.5$. After one cycle of circular waves, the wavefront breaks down and produces four petals, with the size of each petal varying over time, as depicted in Fig. 8C.

In the tilted Petri dish experiment shown in Fig. S5A-B, we adjusted the model to include a term proportional to the height $h(x) = x/N_x$ which varies linearly with x , under the assumption that the fluid height changes solely in the x -direction:

$$\frac{du}{dt} = D\nabla^2 u + \frac{1}{\epsilon}(aw - uw + u - u^2 + p_1 h(x)), \quad (4)$$

$$\frac{dv}{dt} = u - v + p_2 h(x), \quad (5)$$

$$\frac{dw}{dt} = \frac{1}{\epsilon'}(-aw - uw + bv + p_3 h(x)), \quad (6)$$

where $p_1 = p_2 = p_3 = 0.01$.

Supplemental Figures

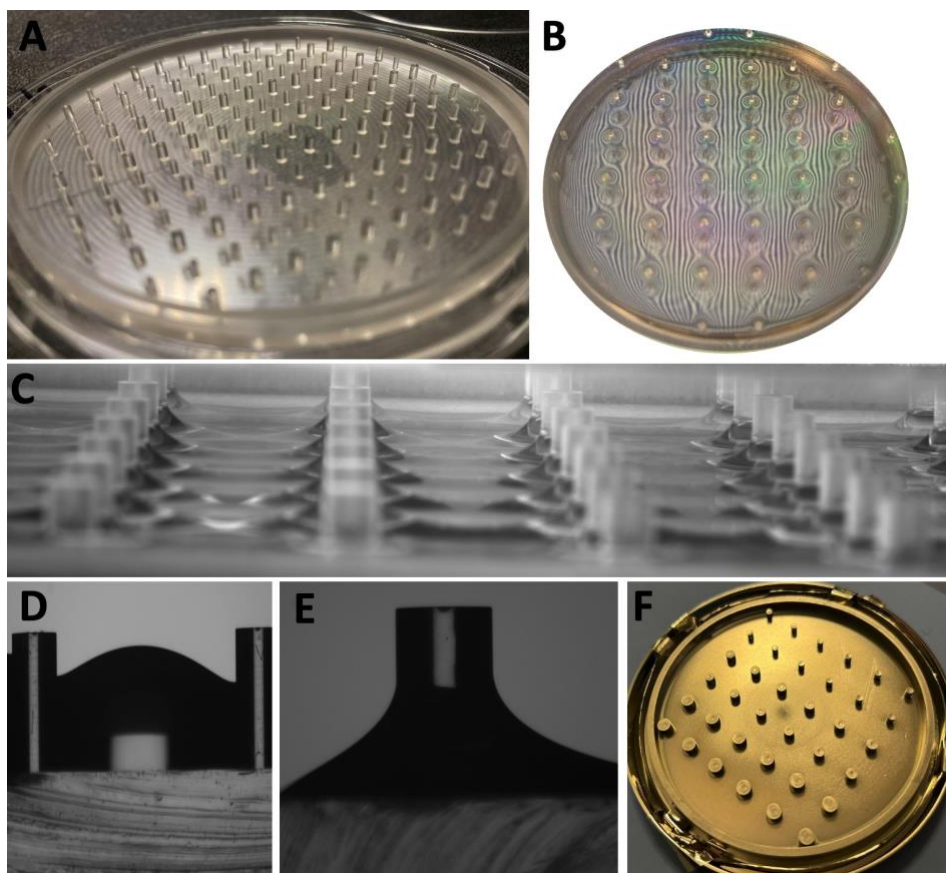


Figure S1: **Experimental design.** (A) A PDMS mold featuring alternating pillar diameters of 1 mm and 1.5 mm was utilized in the experiment shown in Fig. 2. The PDMS mold includes both pillars and PDMS walls around the edges, tailored to fit a standard 100 mm Petri dish. (B) A striped pattern is projected onto the fluid surface to illustrate the deformation caused by the hydrophilic pillars. (C) A side view of a plasma-treated setup is shown when filled with the chemical solution. The pillar diameter is 1.95 mm. (D-E) The profile of the fluid near the pillars is shown before and after plasma treatment. The pillar diameter is 1 mm. (F) A sample of a PDMS mold that has been coated with a thin layer of gold. Large pillars are 3.8 mm in diameter.

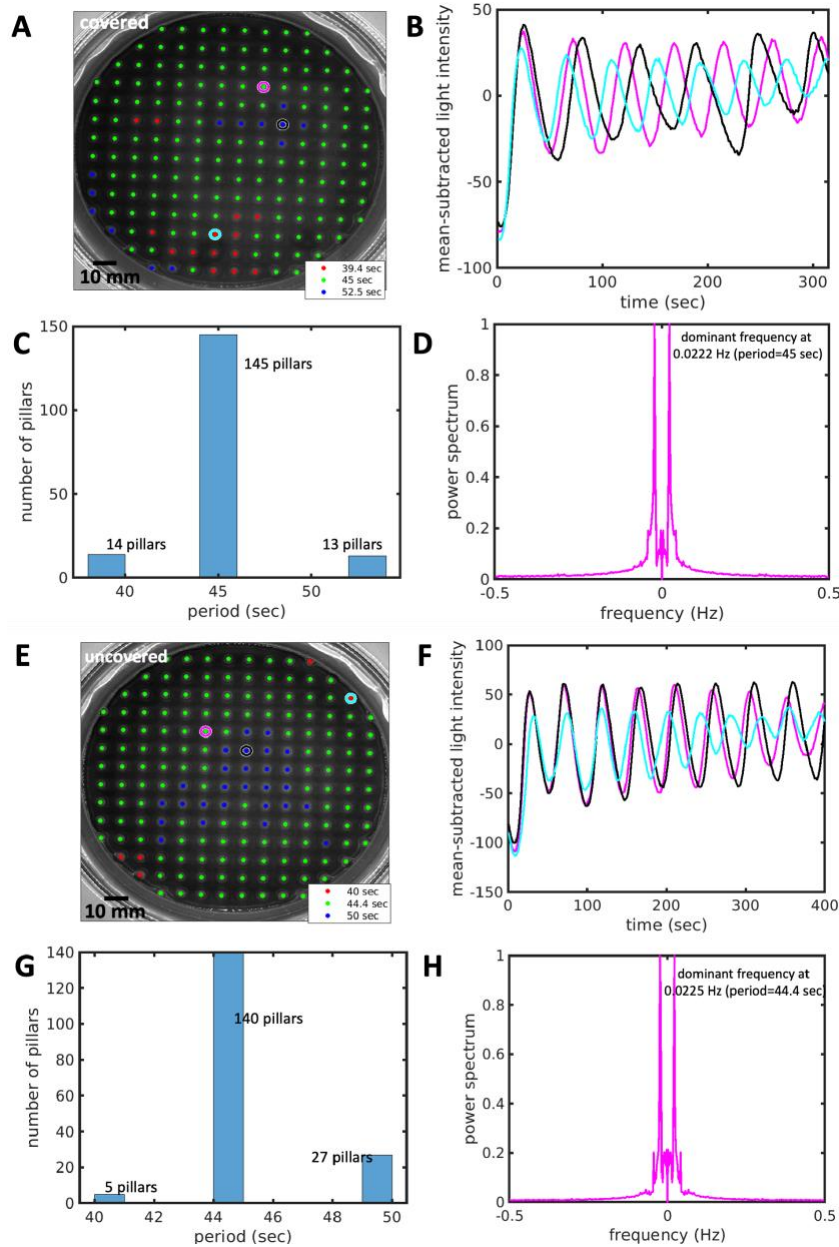


Figure S2: **Frequency Analysis.** (A) Color-coded period of the waves centered around the obstacles, measured in seconds. The Petri dish is covered and the waves maintain their circular shapes over multiple cycles, as shown in Fig. 1K. (B) Averaged light intensity oscillations around three selected pillars highlighted in panel A, showing oscillations with periods of 45 seconds (magenta), 52.5 seconds (black), and 39.4 seconds (cyan). (C) Histogram of oscillations period. (D) Power spectrum of the oscillations shown in magenta in panel (B). (E-H) Similar to panels (A-D), but with the Petri dish uncovered, affecting the wave dynamics as shown in Fig. 1L.

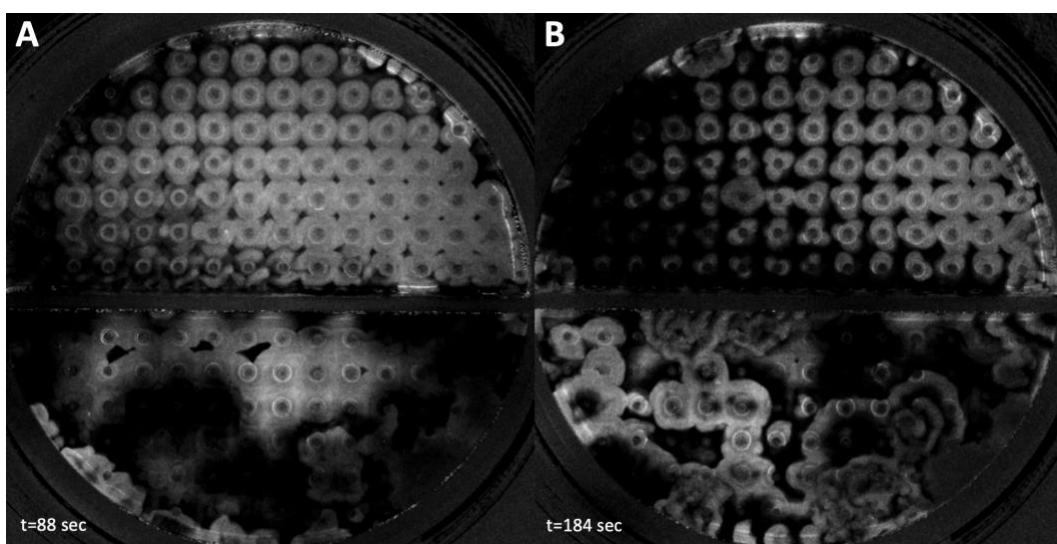


Figure S3: **Hydrophilic versus hydrophobic obstacles:** An overview of a partitioned, uncovered Petri dish taken at two distinct times: before (A) and after (B) the emergence of instability. The upper portion of the dish has been plasma-treated to render PDMS hydrophilic, whereas the lower section has been left untreated, maintaining its hydrophobic properties.

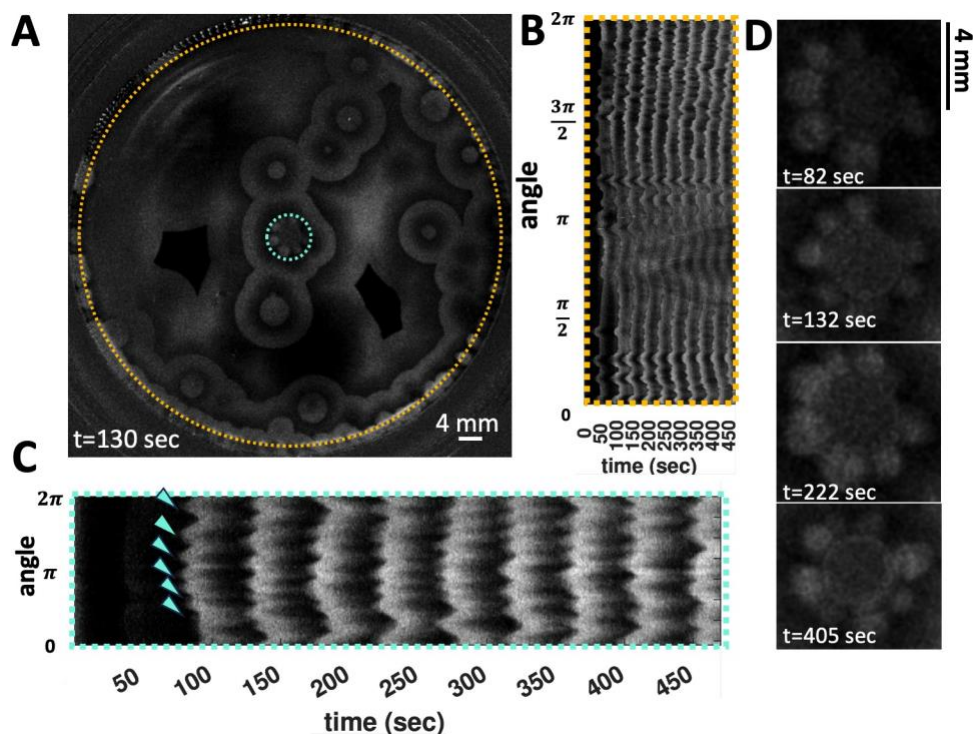


Figure S4: **A single pillar also acts as the wave center.** (A-C) An isolated pillar serves as the wave center and exhibits wavefront instability in an uncovered Petri dish. Additionally, we observe wavefront instability at the PDMS walls around the periphery. (D) shows a flower-like pattern with six or seven petals at different time points that formed around the solitary central pillar.

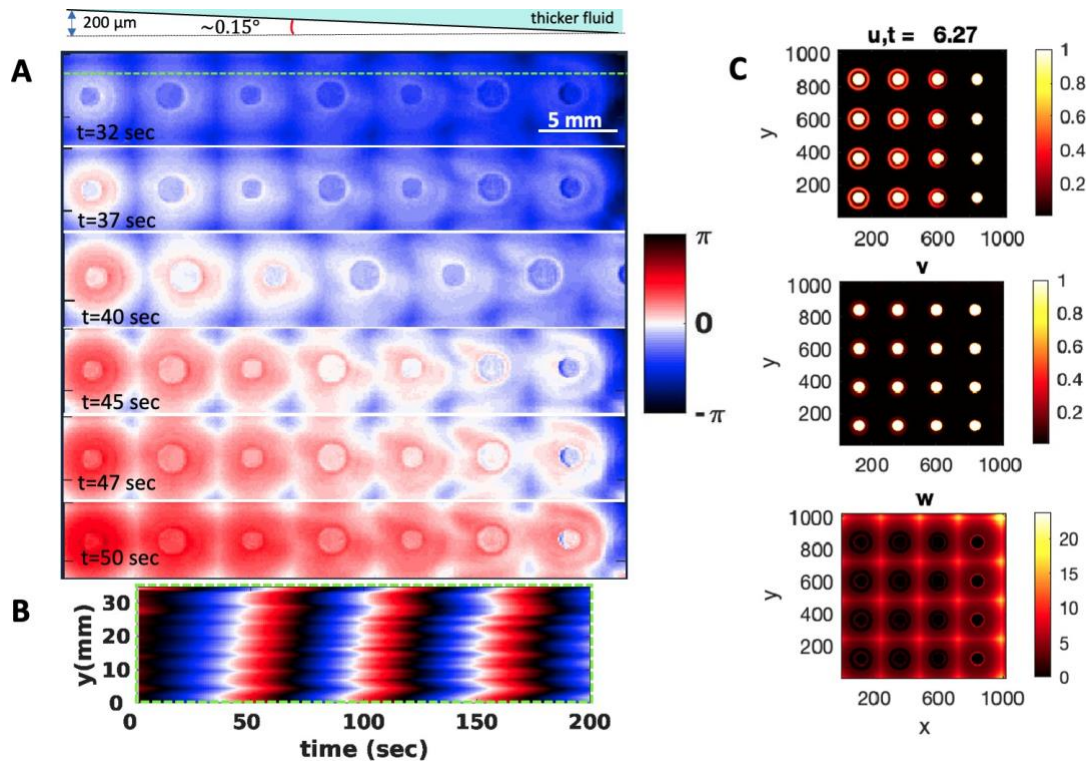


Figure S5: **Experiment in a tilted Petri dish (A)** In a Petri dish with a slight tilt, synchronization waves initiate in the thinner part of the fluid and propagate towards the area with greater fluid thickness. **(B)** Space-time plot of the phase map along the green dashed line indicated in panel (A) illustrates the propagation of phase waves. Notice that in this experiment, the Petri dish is not covered, and flower patterns emerge at $t \sim 80$ sec. **(C)** Numerical simulations emulating the experimental setup shown in panel (A).

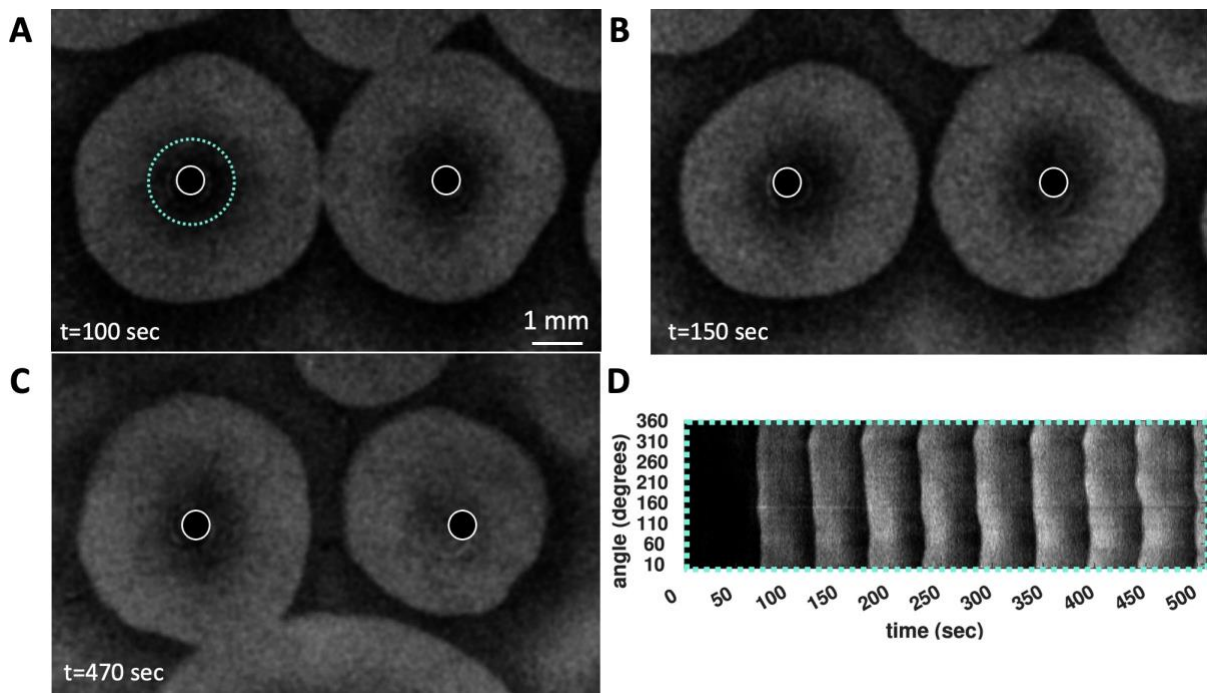


Figure S6: **No fingering instability in small diameter pillars.** (A-D) In experiments conducted with uncovered Petri dishes featuring pillars of 0.5 mm diameter, there is no occurrence of wavefront instability. This observation indicates that a certain minimum perimeter of the pillars is necessary for fingering instability to occur. The space-time plot shown in panel (D) is created by accumulating the light intensity around the cyan-colored circle depicted in panel (A).

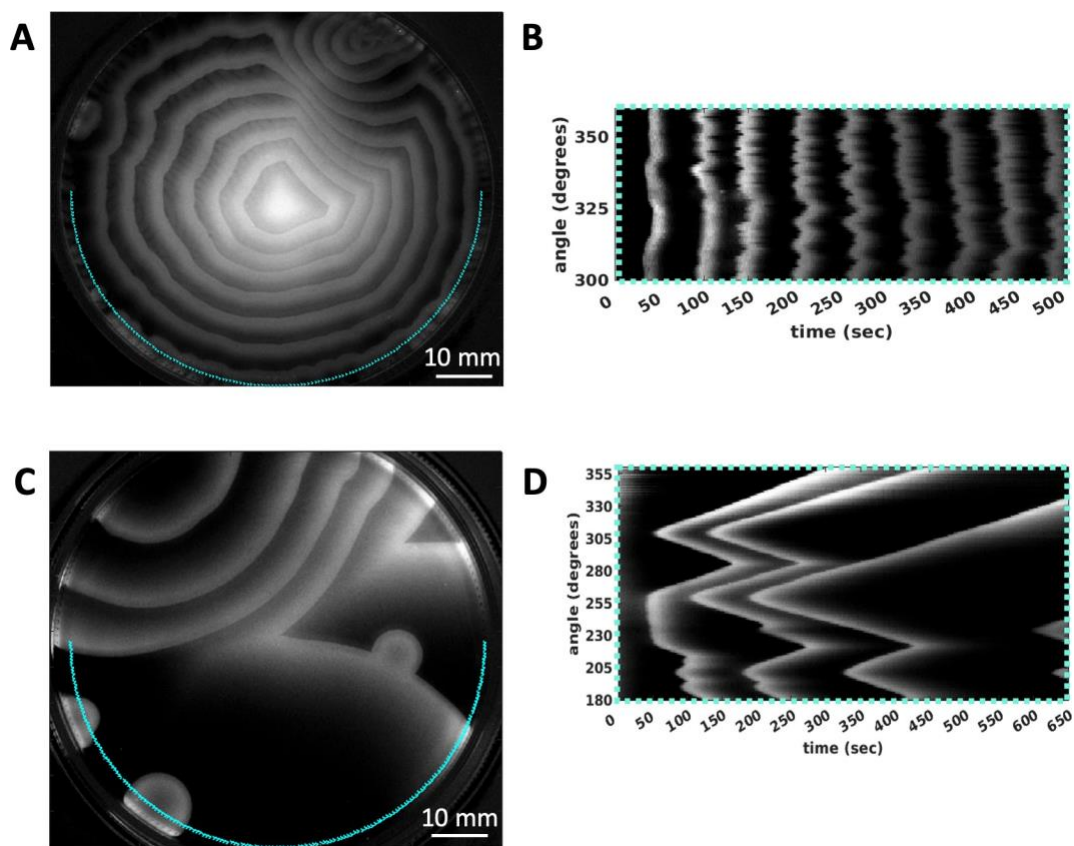


Figure S7: **Experiment in a glass Petri dish without obstacles.** (A) A top view of a glass uncovered Petri dish with plasma treatment, illustrating fingering instability at the glass boundary. Notice that rippled waves travel and make visible the underlying mosaic patterns generated by the Marangoni instabilities. (B) A space-time plot along the cyan-colored semicircle shows the dynamics of the fingering, emphasizing that the positions of the fingers can change over time. (C-D) A setup similar to panel (A), but covered to minimize evaporation. In this configuration, wave centers appear at the periphery, but the wavefronts maintain their circular forms.

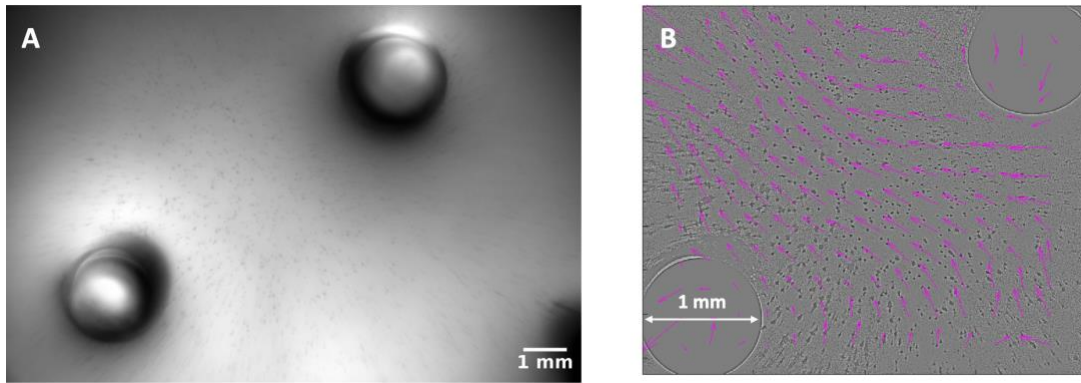


Figure S8: **Marangoni-driven surface flows.** **A-B)** In this experiment, tracer particles ($20\ \mu\text{m}$ in diameter) are utilized to visualize surface flows driven by Marangoni effects, which are caused by gradients in chemical concentration as well as temperature, creating surface tension gradients (refer to video 12).

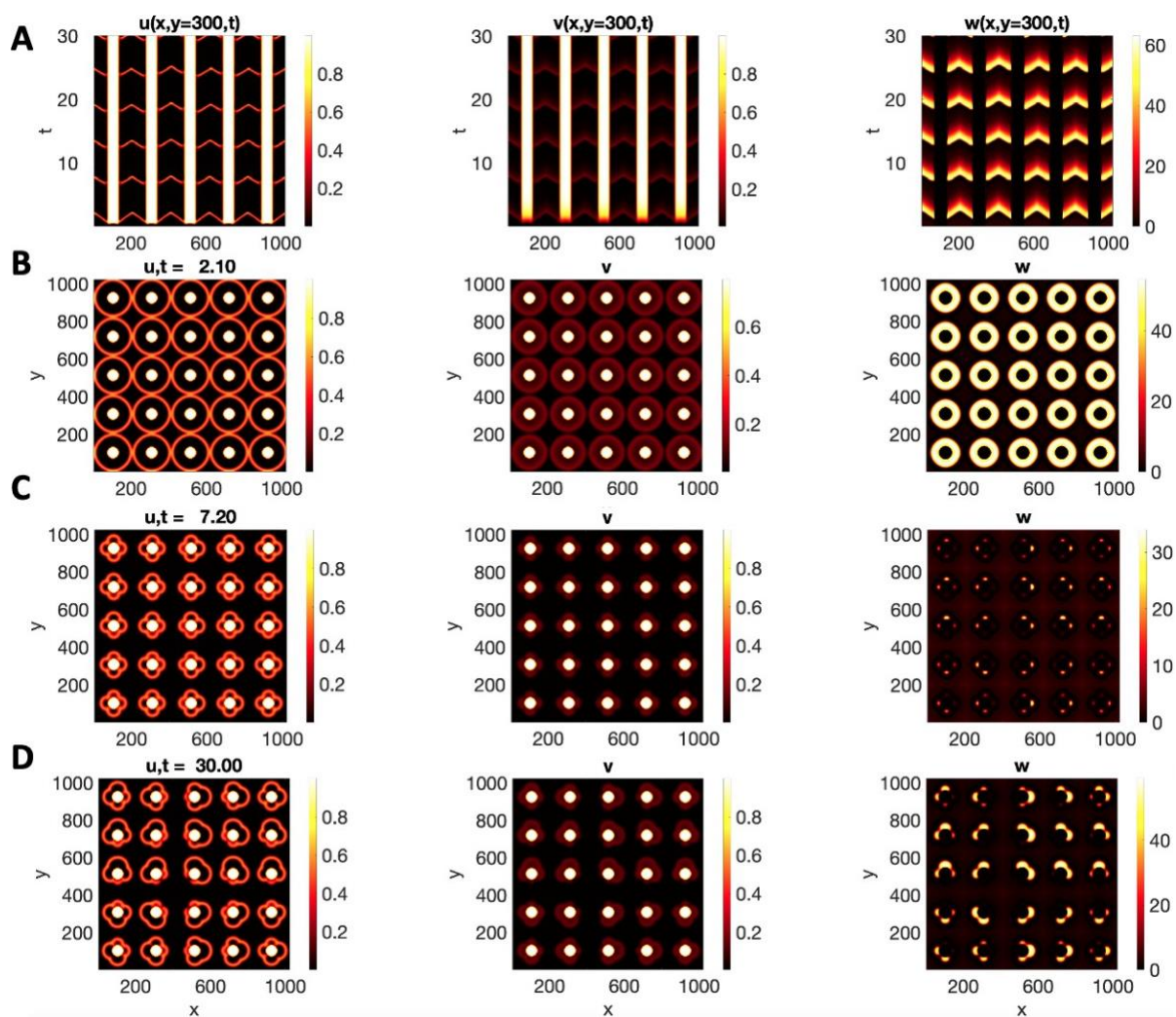


Figure S9: **Numerical simulations with asymmetric w around the pillar.** (A) The space-time plot along the line marked in panel (B) illustrates that the obstacles become wave centers. (B) shows an image of the circular waves emanating from the obstacles. (C-D) Over time, the wavefront breaks, leading to the emergence of flower-like wave patterns.